

Visual Space Is Represented by Nonmatching Topographies of Distinct Mouse Retinal Ganglion Cell Types

Adam Bleckert,^{1,2} Gregory W. Schwartz,³ Maxwell H. Turner,^{1,3} Fred Rieke,^{3,4} and Rachel O.L. Wong^{2,*}

¹Graduate Program in Neurobiology and Behavior

²Department of Biological Structure

³Department of Physiology and Biophysics

University of Washington, Seattle, WA 98195, USA

⁴Howard Hughes Medical Institute, Seattle, WA 98195, USA

Summary

The distributions of neurons in sensory circuits display ordered spatial patterns arranged to enhance or encode specific regions or features of the external environment. Indeed, visual space is not sampled uniformly across the vertebrate retina. Retinal ganglion cell (RGC) density increases and dendritic arbor size decreases toward retinal locations with higher sampling frequency, such as the fovea in primates and area centralis in carnivores [1]. In these locations, higher acuity at the level of individual cells is obtained because the receptive field center of a RGC corresponds approximately to the spatial extent of its dendritic arbor [2, 3]. For most species, structurally and functionally distinct RGC types appear to have similar topographies, collectively scaling their cell densities and arbor sizes toward the same retinal location [4]. Thus, visual space is represented across the retina in parallel by multiple distinct circuits [5]. In contrast, we find a population of mouse RGCs, known as alpha or alpha-like [6], that displays a nasal-to-temporal gradient in cell density, size, and receptive fields, which facilitates enhanced visual sampling in frontal visual fields. The distribution of alpha-like RGCs contrasts with other known mouse RGC types and suggests that, unlike most mammals, RGC topographies in mice are arranged to sample space differentially.

Results and Discussion

Mouse ON Alpha-like RGCs Display a Nasal to Temporal Gradient in Cell Density and Dendritic Arbor Size

Alpha-like mouse retinal ganglion cells (RGCs) segregate into three populations: ON-sustained (A_{ON-S}), OFF-transient (A_{OFF-T}), and OFF-sustained (A_{OFF-S}) [7–10]. Alpha RGCs are readily identified by labeling neurofilaments [11], and in mouse, the antibody SMI-32 directed against nonphosphorylated neurofilament heavy chain readily labels A_{ON-S} and A_{OFF-T} alpha-like RGCs, but not A_{OFF-S} (Figures 1A and 1B; Movie S1 available online) [12, 13]. When we systematically mapped the distributions of A_{ON-S} RGCs labeled by SMI-32, we found a pronounced gradient in their density (>3-fold difference) increasing from nasal to temporal retina, peaking at a temporal-dorsal location (Figures 1A, 1B, and S1). We then reconstructed the individual arbors of SMI-32-labeled A_{ON-S} RGCs using the *Thy1-YFPH* transgenic line [14], in which RGCs are sparsely labeled, and found that the increase in A_{ON-S} RGC density is paralleled by a reduction in dendritic

arbor size (Figures 1C and S2). Quantification of the dendritic arbors revealed that the size of each A_{ON-S} RGC, represented by the diameter of a circle with an area equivalent to its arbor area (see the Supplemental Experimental Procedures), scaled linearly across the nasal-temporal axis of the retina (Figure 1D), whereas no relationship existed between arbor size and retinal eccentricity from the optic nerve head (Figure 1E). Previously, mouse RGC types have been believed to be relatively uniformly distributed across the retina and have largely been classified according to soma and dendritic arbor size, branching patterns, and stratification level [9, 12, 15–19], unless a molecular-marker was available [13, 20–24]. Based on these criteria, the alpha-like RGCs in different retinal regions were likely classified as distinct cell types in previous studies (see Table S1).

Further quantification of A_{ON-S} RGCs indicated that their arbor size is proportional to total dendritic length, whereas soma size is uniform across cells (Figures 1F and 1G). A_{ON-S} arbor size also correlated with mean dendritic segment length, but not with the total number of dendritic segments (Figures 1H and 1I). To compare the branching patterns of A_{ON-S} RGCs across the retina, we quantified dendritic branch number as a function of distance from the soma by calculating the number of Sholl intersections (Figure 1J). We found that the Sholl curves of A_{ON-S} RGCs across retinal locations overlapped when normalized by their dendritic diameter size (Figure 1K; see the Supplemental Experimental Procedures). This suggests that A_{ON-S} RGCs simply scale up or down their dendritic arbors to increase or decrease their dendritic territory depending upon their position in the retina. These differences in size may be dictated by the local density of A_{ON-S} RGCs, because homotypic interactions are known to regulate the dendritic territories of other mouse retinal neurons [25–29]. Furthermore, manipulations to increase the total RGC density in cat retinas cause a decrease in alpha RGC size [30]. However, homotypic regulation may not be consistent across all retinal neurons in mice [31].

A_{ON-S} RGCs across the Retina Are Arranged in Mosaic Distributions and Have Similar ON-Sustained Responses to Light

To further confirm that the SMI-32-labeled A_{ON-S} RGCs represent variations of a single type of RGC, we performed two additional sets of experiments. First, we determined whether these cells exhibit a mosaic distribution, a feature delineating separate cell types in the retina. We mapped the distribution of A_{ON-S} RGCs in 1 mm² regions of nasal and temporal retina and calculated their density recovery profile (Figures 2 and S1; see the Supplemental Experimental Procedures). Populations in both regions displayed a zone of exclusion indicated by a decreased cell density near a reference cell; such an exclusion zone is a hallmark of cells distributed in a mosaic pattern [32]. The effective radius of this exclusion and the nearest neighbor distances in nasal retina were greater than those in temporal retina (Figure 2B). Second, we measured the light responses of A_{ON-S} RGCs by recording whole-cell currents in response to brief steps of light from darkness (see the Supplemental Experimental Procedures). Cells in both temporal and nasal regions showed sustained excitatory and inhibitory currents in response to light onset, physiological hallmarks of

*Correspondence: wongr2@uw.edu

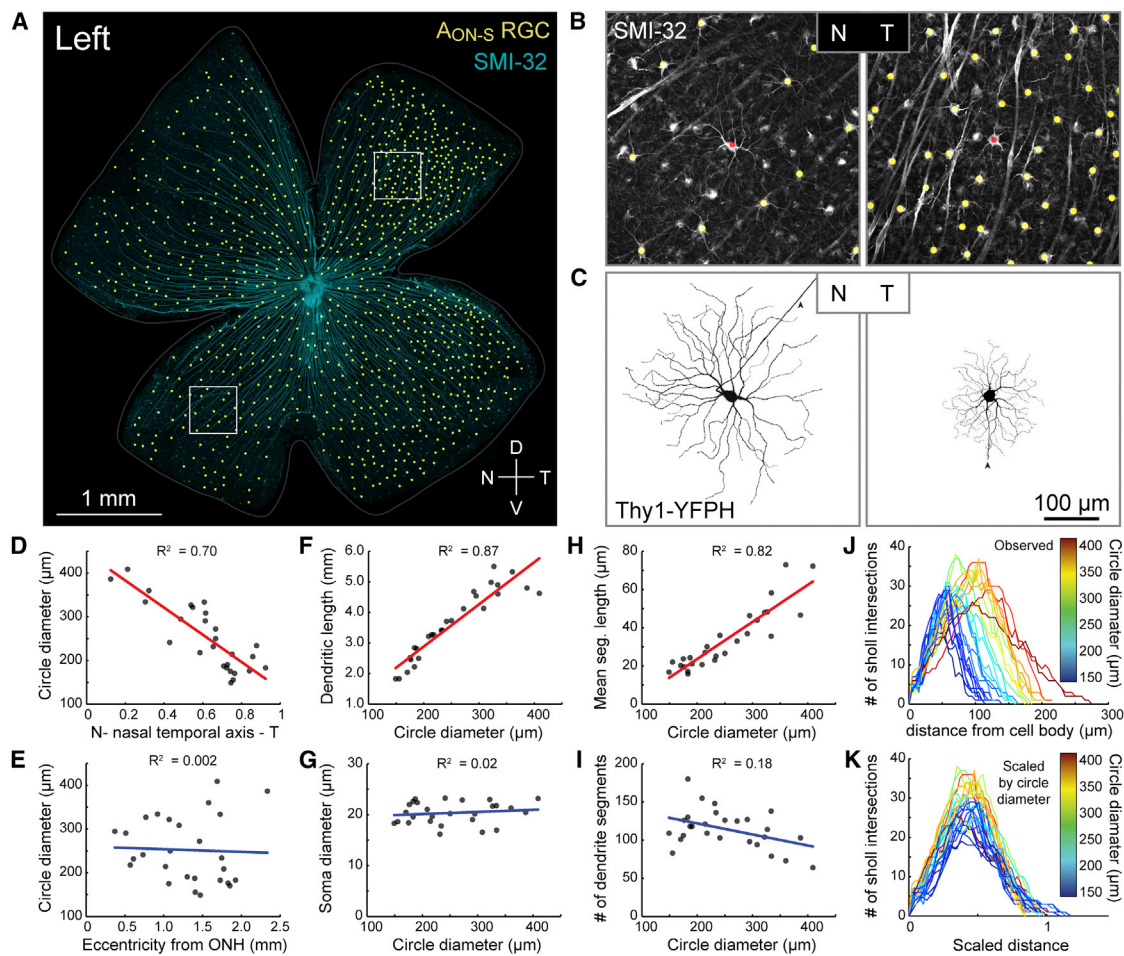


Figure 1. Cell Density and Size of AON-S Retinal Ganglion Cells Form Inverse Gradients across the Mouse Retina

(A) Locations of AON-S RGCs (yellow dots) labeled by SMI-32 immunostaining (cyan) in a whole-mount retina (left eye) from a P24 mouse (V, ventral; D, dorsal; N, nasal; T, temporal). (B) Maximum intensity projections of image stacks encompassing SMI-32-labeled RGC somata and primary dendrites (gray) within the boxed regions in (A). AON-S RGCs are identified by their relatively brighter cell bodies and dendrite labeling (yellow dots). (C) Sparse labeling of AON-S RGCs in *Thy1-YFPH* transgenic mice enables visualization of the complete dendritic arbors of individual SMI-32 RGCs (red dots in B). Arrowhead demarcates RGC axon. (D) Dendritic arbor sizes of AON-S RGCs represented by diameters of circles with areas equivalent to the arbor area (see the [Supplemental Experimental Procedures](#)) are plotted across nasal-temporal retina. (E–K) Relationships between AON-S RGC size (circle diameter) and retinal eccentricity from the optic nerve head (ONH) (E), total dendritic length (F), soma size (G), mean segment length (H), and number of dendritic segments (I). (J) Number of Sholl intersections as a function of the distance from the soma for each cell, and (K) Sholl intersections after normalizing the curves according to dendritic arbor size. ($n = 2$ retinas, 27 RGCs). See also [Figures S1](#) and [S2](#), [Table S1](#), and [Movie S1](#).

AON-S RGCs [7, 10, 33]. The retinas were fixed after electrophysiology, and the recorded cells were subsequently confirmed to be SMI-32 positive ($n = 11$ out of 11 cells, 5 T and 6 N). Furthermore, nearest neighbor distributions confirmed that recorded small-arbor cells were in temporal retina, whereas large-arbor cells were located in nasal retina (examples; [Figures 2C](#) and [2D](#)). Our structural and functional analyses therefore together uncovered a single population of RGC in the mouse retina resembling the ON-alpha RGC populations in other species [6].

Visual Space in Temporal Retina Has an Enhanced Sampling by AON-S RGCs, but Not by Their Dominant Presynaptic Partners

Why might AON-S RGCs have an increased density in temporal retina? To gain insight, we first asked whether the dominant

excitatory presynaptic partner of AON-S RGCs [34], the type 6 cone bipolar cell (T6 BC) also scales its axonal field proportionally to the AON-S RGCs dendritic arbor. Surprisingly, we found no change in the distribution of T6 BC axon sizes in nasal compared to temporal retina ([Figure 3A](#)). Thus, in this circuit, the presynaptic T6 BCs maintain a uniform sampling of visual space across the retina, whereas the postsynaptic AON-S RGCs bias their sampling toward temporal retina. This is in contrast to species with specialized areas of central vision, where bipolar and ganglion cells both scale toward areas of peak density [1, 35].

To quantify how the change in size and density of AON-S RGCs could affect sampling of the visual field, we first calculated their dendritic coverage factor ([Figures 3B](#) and [3C](#); see the [Supplemental Experimental Procedures](#)). In temporal retina, dendritic coverage of AON-S RGCs is 1.3 times greater

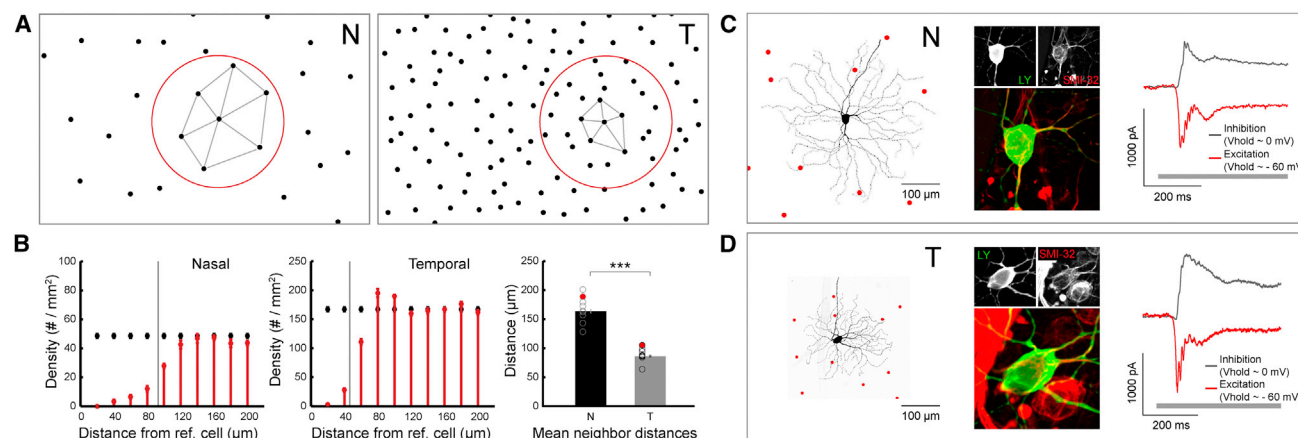


Figure 2. AON-S RGCs Have Mosaic Distributions and Characteristic ON Sustained Responses to Light Stimuli

(A) Example spatial distributions of AON-S RGCs (black dots), sampled from nasal (N) and temporal (T) retina. The density recovery profile (DRP) was calculated using a 200 μm radius (red circles). Nearest neighbor distances (gray lines) were calculated for every RGC within a region. (B) DRP plots of AON-S RGCs as a function of distance from the reference cell (red) compared to the DRP of cells with a random distribution (black). The effective radius of exclusion for nasal regions is greater than for temporal (gray vertical lines, $N = 93.2$, $T = 46.5$ μm , $p < 0.0002$), but the packing factor was not ($T = 0.31$, $N = 0.36$, $p = 0.10$). The average nearest neighbor distance is greater in nasal compared to temporal retina ($N = 168.0$, $T = 88.4$ μm , $p < 0.0002$). $n = 8$ retinas for all measures. (C) Left: an example AON-S RGC targeted for electrophysiological recording in nasal retina. Dendritic arbors were visualized upon cell filling with Lucifer yellow (LY), and neighboring AON-S RGCs (red dots) were identified subsequently by SMI-32 labeling. Mean neighbor distances for the recorded cell are displayed as red in (B, right). Middle: targeted AON-S RGCs showing colabeling of LY and SMI-32. Right: excitatory (red traces) and inhibitory (gray traces) currents show characteristic sustained responses to light stimuli (gray bar, 500 ms). (D) An example AON-S RGCs targeted in temporal retina show the same characteristic responses as in nasal retina. Data are shown as mean \pm SEM. See also Figure S1.

than in nasal retina (Figure 3D); i.e., any point in the retina is sampled, on average, by more AON-S RGCs in temporal versus nasal retina. We next compared this dendritic coverage to the functional coverage of AON-S RGCs by mapping the receptive field sizes for targeted AON-S RGCs across the retina. The receptive field size of AON-S RGCs does not parallel dendritic field size; temporal AON-S RGCs have greater receptive field size than their dendritic field size, whereas nasal AON-S RGC dendritic and receptive field sizes appear more similar (Figure 3E; see the Supplemental Experimental Procedures). This increase in receptive field size results in a further enhancement (2.2 times) in coverage of the visual field by AON-S RGCs in temporal compared to nasal retina (Figure 3F). Thus, each AON-S RGC in temporal retina not only encodes a smaller unit of visual space than in nasal retina, but also every point in space is sampled by a greater number of AON-S RGCs.

What function might a population of RGCs with enhanced visual sampling in temporal retina serve? In rodents, ipsilateral projecting RGCs that underlie binocular vision are located in temporal retina [36, 37], and alpha-like RGCs are overrepresented, $\sim 10\%$ of RGCs in the ipsilateral projecting population, whereas they constitute only $\sim 1\%$ of the total RGC population [36, 38]. Furthermore, the location of peak density of AON-S RGCs is near the center of the rodent frontal visual fields (Figures 4A and 4B) [36, 37, 39, 40]. The mouse retina has commonly been believed to have a relatively uniform distribution of cell types across the retina [15, 42], and a cell type with a temporal-nasal gradient similar to those found in animals with clear binocular vision [11, 44] is unexpected for mice. In addition to previous work showing alpha-like RGCs are adept at detecting fine-scale spatial patterns [34], processing chromatic information [45], and possibly displaying intrinsic photosensitivity [46, 47], our work places AON-S RGCs in this unique location specialized for encoding frontal vision.

The Distributions of ON and OFF Alpha-like RGCs Differ from Those of Other Known Mouse RGCs and Suggest an Independent Sampling of Visual Space by Distinct RGC Types

We next asked if the two known OFF alpha-like RGCs found in mouse also display similar distributions to ON alpha-like RGCs [7, 10]. We observed one OFF population of RGCs that varied in dendritic arbor size between nasal and temporal retina, in a manner paralleling AON-S RGCs. The dendritic stratification and morphology of these cells are characteristic of AOFF-S RGCs [7, 10] (Figure S2). This suggests that AOFF-S RGCs are also organized for enhanced sampling of visual space in temporal retina. Conversely, we found that the distribution of SMI-32-labeled AOFF-T RGCs varied much less across the retina (Figure S1) in contrast to most mammals [6], although similar to other rodents [48], which may be accompanied by some change in dendritic field size [13, 49]. Taken together, our current mapping of the topographic distributions of cell densities and dendritic arbor sizes of alpha-like RGCs strongly contrasts with that of known mouse RGCs (Figures 4C and 4D). Previous studies demonstrated a peak in W3 RGCs (presumed local edge detector) in ventral retina [22], an increased density of M1 and M2 RGCs (intrinsically photosensitive) in dorsal retina [23], and relatively flatter distributions for direction-selective RGC types, such as JAM-B [19, 20], DRD4 [21, 50], BD RGCs [19, 21], and Hoxd10 [24]. This raises a striking difference between the mouse retina and that of other mammals, whereby diverse RGC types in the mouse appear to exhibit distinct topographies and have adopted a strategy to customize the distributions of each RGC type to sample the visual environment.

Conclusions

In summary, our findings suggest that sampling of the visual scene by AON-S RGCs is modulated across the retina by a

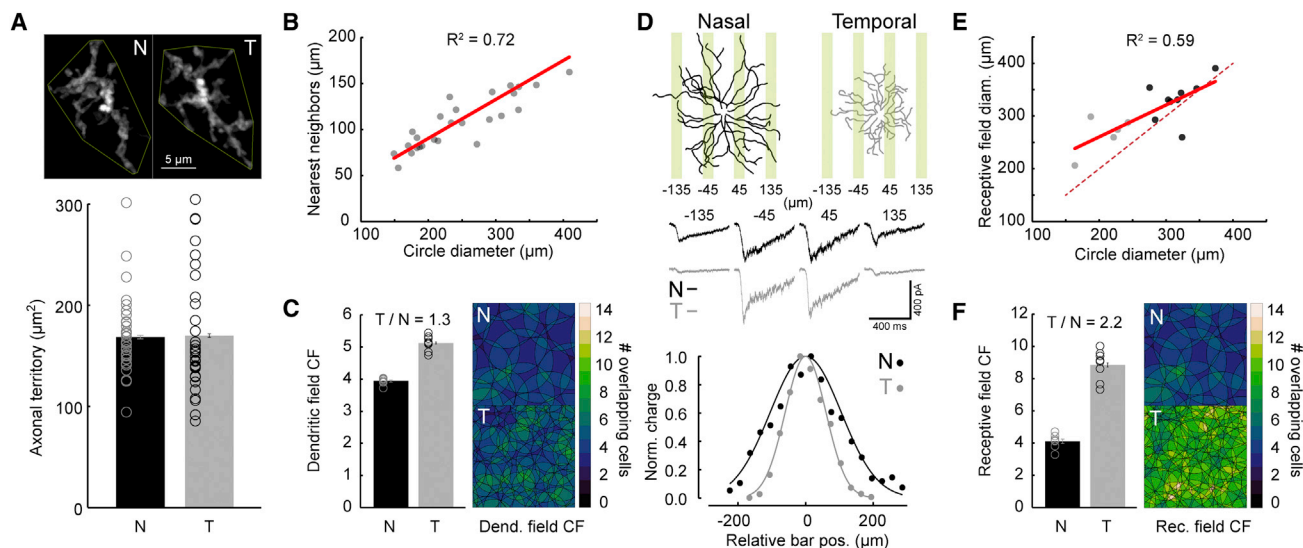


Figure 3. Increased Density of A_{ON-S} RGCs in Temporal Retina Results in an Enhanced Sampling of the Visual Field, which Is Not Paralleled by Their Dominant Presynaptic Partner

(A) Axonal terminals of nasal (N) and temporal (T) located type 6 bipolar cells visualized by expression of tdTomato in the *Grm6-tdTomato* mouse (see the [Supplemental Experimental Procedures](#)). Their axonal territory sizes (area of the polygon) are plotted here for cells in nasal and temporal retina. ($n = 4$ retinas, 37 N and 34 T cells).

(B) Plot of the diameter of A_{ON-S} RGC dendritic arbors against mean nearest neighbor distances.

(C) Dendritic field coverage factor (CF) of A_{ON-S} RGCs in nasal and temporal retina (CF_N = 3.9, CF_T = 5.1). Coverage factor (colored) maps were calculated from maps of A_{ON-S} RGCs dendritic field overlap predicted from their neighbor distances (B; see the [Supplemental Experimental Procedures](#)).

(D) Top: example dendritic fields from A_{ON-S} RGCs targeted across the retina, whose receptive field diameters were mapped using sequential bars of light (see the [Supplemental Experimental Procedures](#)). Middle: average excitatory current traces from example nasal (black) and temporal (gray) cells recorded in response to light stimuli at the indicated bar positions. Bottom: response profiles were fit to the normalized charge transfers (dots) with Gaussian functions (smooth curves).

(E) Dendritic diameters of A_{ON-S} RGCs were reconstructed from the recorded cells and plotted against their respective receptive field diameters (see the [Supplemental Experimental Procedures](#)) ($n = 14$ cells). Receptive fields of temporal cells (gray dots) are larger than their dendritic fields ($p = 0.03$) (dashed red line shows unity), but the two measures appear similar for nasal cells (black dots, $p = 0.4$) (see the [Supplemental Experimental Procedures](#)).

(F) Receptive field CF of A_{ON-S} RGCs in nasal and temporal retina (CF_N = 4.1, CF_T = 8.8). Coverage factor maps were calculated for the same nasal and temporal regions in (C).

Data are shown as mean \pm SEM.

nonuniform topographic distribution of their densities and receptive field sizes, distinct from the topographic patterns of other known mouse RGC types. The diversity of RGC distributions in the mouse retina suggests that visual space is not sampled uniformly by parallel processing circuits across the retina in mice, but instead distinct populations of RGCs may be organized in separate topographies to encode specific visual features or regions [20, 22, 23, 50, 51].

Supplemental Information

Supplemental Information includes Supplemental Experimental Procedures, two figures, one table, and one movie and can be found with this article online at <http://dx.doi.org/10.1016/j.cub.2013.12.020>.

Acknowledgments

Funded by NIH EY10699 (R.O.L.W.), NIH Developmental Biology Training Grant T32HD007183 and Neurobiology and Behavior Training Grant 5 T32 GM07108 (A.B.), NEI Vision Training Grant EY07031 (M.H.T.), Howard Hughes Medical Institute (F.R.), and Helen Hay Whitney Foundation Fellowship (G.W.S.). We would like to thank Felice Dunn and Luca Della Santina for many helpful discussions and comments on the manuscript.

Received: October 29, 2013

Revised: December 10, 2013

Accepted: December 10, 2013

Published: January 16, 2014

References

- Wässle, H., and Boycott, B.B. (1991). Functional architecture of the mammalian retina. *Physiol. Rev.* 71, 447–480.
- Peichl, L., and Wässle, H. (1983). The structural correlate of the receptive field centre of alpha ganglion cells in the cat retina. *J. Physiol.* 341, 309–324.
- Yang, G., and Masland, R.H. (1994). Receptive fields and dendritic structure of directionally selective retinal ganglion cells. *J. Neurosci.* 14, 5267–5280.
- Collin, S.P. (2008). A web-based archive for topographic maps of retinal cell distribution in vertebrates. *Clin. Exp. Optom.* 91, 85–95.
- Field, G.D., and Chichilnisky, E.J. (2007). Information processing in the primate retina: circuitry and coding. *Annu. Rev. Neurosci.* 30, 1–30.
- Peichl, L. (1991). Alpha ganglion cells in mammalian retinas: common properties, species differences, and some comments on other ganglion cells. *Vis. Neurosci.* 7, 155–169.
- Pang, J.J., Gao, F., and Wu, S.M. (2003). Light-evoked excitatory and inhibitory synaptic inputs to ON and OFF alpha ganglion cells in the mouse retina. *J. Neurosci.* 23, 6063–6073.
- Schubert, T., Degen, J., Willecke, K., Hormuzdi, S.G., Monyer, H., and Weiler, R. (2005). Connexin36 mediates gap junctional coupling of alpha-ganglion cells in mouse retina. *J. Comp. Neurol.* 485, 191–201.
- Völgyi, B., Abrams, J., Paul, D.L., and Bloomfield, S.A. (2005). Morphology and tracer coupling pattern of alpha ganglion cells in the mouse retina. *J. Comp. Neurol.* 492, 66–77.
- van Wyk, M., Wässle, H., and Taylor, W.R. (2009). Receptive field properties of ON- and OFF-ganglion cells in the mouse retina. *Vis. Neurosci.* 26, 297–308.

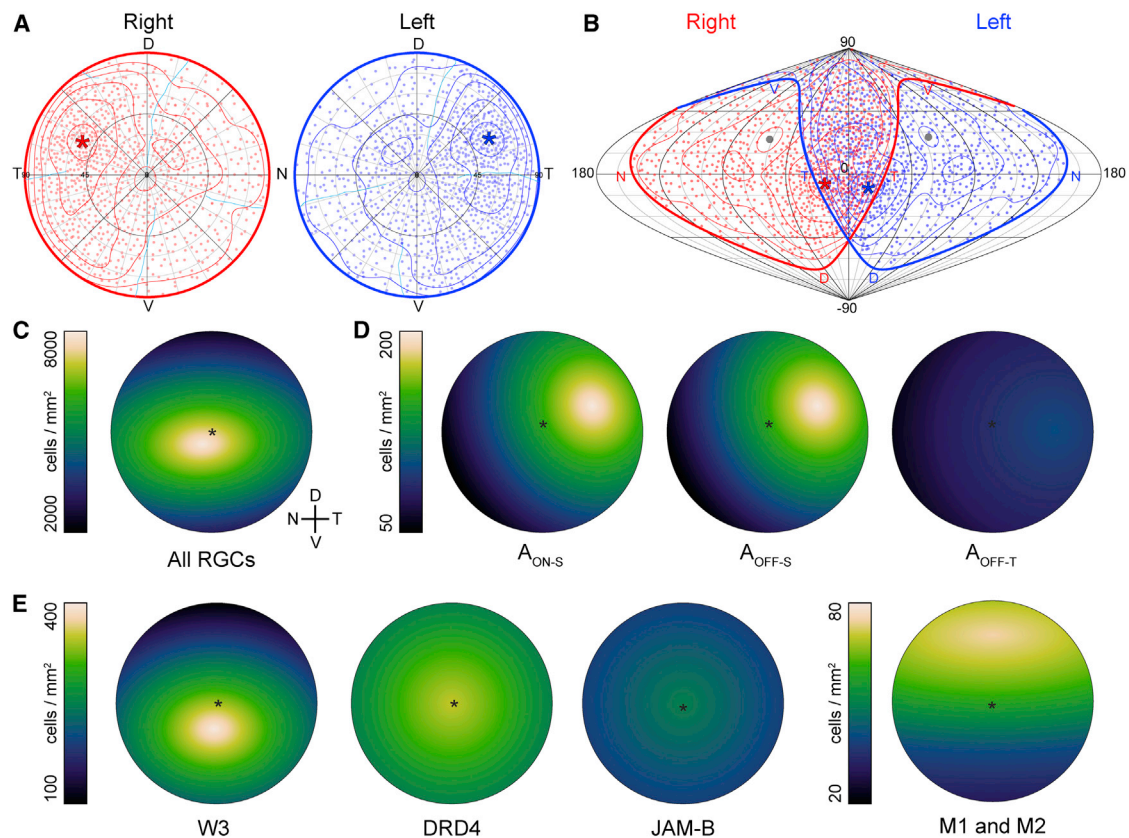


Figure 4. Sampling of Frontal Visual Space Is Enhanced in A_{ON-S} RGC Distributions, which Contrast with the Distributions of Known RGC Types

(A) Azimuthal equilateral projections of retina space for A_{ON-S} RGC distributions from right (red) and left (blue) eyes shown in Figures 1 and S1, reconstructed and plotted using the Retistruct package [40]. Isodensity lines demarcate 5%, 25%, 50%, 75%, and 95% contours of the peak density located at the asterisk (~ 180 cells/mm²). Cyan lines delineate computed sutures of the original relief cuts made for flat-mount preparation.

(B) Sinusoidal projection of mouse visual space for A_{ON-S} RGC distributions from retinas in (A) (see the Supplemental Experimental Procedures). Red outline represents the edge of the right retina; blue outline represents the edge of the left retina. N, nasal; D, dorsal; V, ventral; T, temporal, indicate the projection of the corresponding pole of the retina. Gray circle represents the position of the optic nerve head. Note the peak densities for right and left retinas (red and blue asterisks) and increased density (75% and 50% isodensity lines) are biased toward the vertical midline (0) corresponding to rostral frontal visual fields of mice.

(C) The density of the total RGC population peaks at a location just nasal and ventral of the optic nerve head (black asterisk) (schematized from [41]; see also [42, 43]).

(D) In contrast, we show here that A_{ON-S} and likely A_{OFF-S} RGCs have peak densities in the temporal-dorsal retina, whereas A_{OFF-T} RGCs are relatively more uniformly distributed across the retina.

(E) Furthermore, the distributions of previously characterized RGCs show varied or flat distributions.

The density color maps in (C) and (E) are schematics based on previously reported RGC densities and changes in dendritic arbor sizes (see the Supplemental Experimental Procedures). Density color maps in (D) are schematics based on the distributions of A_{ON-S} and A_{OFF-T} RGCs shown in Figure S1 and predicted from A_{OFF-S} dendritic arbor sizes illustrated in Figure S2.

See also Figure S2.

- Peichl, L., Ott, H., and Boycott, B.B. (1987). Alpha ganglion cells in mammalian retinas. *Proc. R. Soc. Lond. B Biol. Sci.* 231, 169–197.
- Coombs, J., van der List, D., Wang, G.Y., and Chalupa, L.M. (2006). Morphological properties of mouse retinal ganglion cells. *Neuroscience* 140, 123–136.
- Huberman, A.D., Manu, M., Koch, S.M., Susman, M.W., Lutz, A.B., Ullian, E.M., Baccus, S.A., and Barres, B.A. (2008). Architecture and activity-mediated refinement of axonal projections from a mosaic of genetically identified retinal ganglion cells. *Neuron* 59, 425–438.
- Feng, G., Mellor, R.H., Bernstein, M., Keller-Peck, C., Nguyen, Q.T., Wallace, M., Nerbonne, J.M., Lichtman, J.W., and Sanes, J.R. (2000). Imaging neuronal subsets in transgenic mice expressing multiple spectral variants of GFP. *Neuron* 28, 41–51.
- Sun, W., Li, N., and He, S. (2002). Large-scale morphological survey of mouse retinal ganglion cells. *J. Comp. Neurol.* 451, 115–126.
- Badea, T.C., and Nathans, J. (2004). Quantitative analysis of neuronal morphologies in the mouse retina visualized by using a genetically directed reporter. *J. Comp. Neurol.* 480, 331–351.
- Kong, J.H., Fish, D.R., Rockhill, R.L., and Masland, R.H. (2005). Diversity of ganglion cells in the mouse retina: unsupervised morphological classification and its limits. *J. Comp. Neurol.* 489, 293–310.
- Völgyi, B., Chheda, S., and Bloomfield, S.A. (2009). Tracer coupling patterns of the ganglion cell subtypes in the mouse retina. *J. Comp. Neurol.* 512, 664–687.
- Hong, Y.K., Kim, I.J., and Sanes, J.R. (2011). Stereotyped axonal arbors of retinal ganglion cell subsets in the mouse superior colliculus. *J. Comp. Neurol.* 519, 1691–1711.
- Kim, I.J., Zhang, Y., Yamagata, M., Meister, M., and Sanes, J.R. (2008). Molecular identification of a retinal cell type that responds to upward motion. *Nature* 452, 478–482.
- Kay, J.N., De la Huerta, I., Kim, I.J., Zhang, Y., Yamagata, M., Chu, M.W., Meister, M., and Sanes, J.R. (2011). Retinal ganglion cells with distinct directional preferences differ in molecular identity, structure, and central projections. *J. Neurosci.* 31, 7753–7762.

22. Zhang, Y., Kim, I.J., Sanes, J.R., and Meister, M. (2012). The most numerous ganglion cell type of the mouse retina is a selective feature detector. *Proc. Natl. Acad. Sci. USA* 109, E2391–E2398.
23. Hughes, S., Watson, T.S., Foster, R.G., Peirson, S.N., and Hankins, M.W. (2013). Nonuniform distribution and spectral tuning of photosensitive retinal ganglion cells of the mouse retina. *Curr. Biol.* 23, 1696–1701.
24. Dhande, O.S., Estevez, M.E., Quattrocchi, L.E., El-Danaf, R.N., Nguyen, P.L., Berson, D.M., and Huberman, A.D. (2013). Genetic dissection of retinal inputs to brainstem nuclei controlling image stabilization. *J. Neurosci.* 33, 17797–17813.
25. Reese, B.E., Raven, M.A., and Stagg, S.B. (2005). Afferents and homotypic neighbors regulate horizontal cell morphology, connectivity, and retinal coverage. *J. Neurosci.* 25, 2167–2175.
26. Poché, R.A., Raven, M.A., Kwan, K.M., Furuta, Y., Behringer, R.R., and Reese, B.E. (2008). Somal positioning and dendritic growth of horizontal cells are regulated by interactions with homotypic neighbors. *Eur. J. Neurosci.* 27, 1607–1614.
27. Huckfeldt, R.M., Schubert, T., Morgan, J.L., Godinho, L., Di Cristo, G., Huang, Z.J., and Wong, R.O. (2009). Transient neurites of retinal horizontal cells exhibit columnar tiling via homotypic interactions. *Nat. Neurosci.* 12, 35–43.
28. Lee, S.C., Cowgill, E.J., Al-Nabulsi, A., Quinn, E.J., Evans, S.M., and Reese, B.E. (2011). Homotypic regulation of neuronal morphology and connectivity in the mouse retina. *J. Neurosci.* 31, 14126–14133.
29. Kay, J.N., Chu, M.W., and Sanes, J.R. (2012). MEGF10 and MEGF11 mediate homotypic interactions required for mosaic spacing of retinal neurons. *Nature* 483, 465–469.
30. Kirby, M.A., and Chalupa, L.M. (1986). Retinal crowding alters the morphology of alpha ganglion cells. *J. Comp. Neurol.* 251, 532–541.
31. Lin, B., Wang, S.W., and Masland, R.H. (2004). Retinal ganglion cell type, size, and spacing can be specified independent of homotypic dendritic contacts. *Neuron* 43, 475–485.
32. Rodieck, R.W. (1991). The density recovery profile: a method for the analysis of points in the plane applicable to retinal studies. *Vis. Neurosci.* 6, 95–111.
33. Murphy, G.J., and Rieke, F. (2006). Network variability limits stimulus-evoked spike timing precision in retinal ganglion cells. *Neuron* 52, 511–524.
34. Schwartz, G.W., Okawa, H., Dunn, F.A., Morgan, J.L., Kerschensteiner, D., Wong, R.O., and Rieke, F. (2012). The spatial structure of a nonlinear receptive field. *Nat. Neurosci.* 15, 1572–1580.
35. Chan, T.L., Martin, P.R., Clunas, N., and Grünert, U. (2001). Bipolar cell diversity in the primate retina: morphologic and immunocytochemical analysis of a new world monkey, the marmoset *Callithrix jacchus*. *J. Comp. Neurol.* 437, 219–239.
36. Dräger, U.C., and Olsen, J.F. (1980). Origins of crossed and uncrossed retinal projections in pigmented and albino mice. *J. Comp. Neurol.* 191, 383–412.
37. Reese, B.E., and Cowey, A. (1986). Large retinal ganglion cells in the rat: their distribution and laterality of projection. *Exp. Brain Res.* 67, 375–385.
38. Dreher, B., Sefton, A.J., Ni, S.Y.K., and Nisbett, G. (1985). The morphology, number, distribution and central projections of Class I retinal ganglion cells in albino and hooded rats. *Brain Behav. Evol.* 26, 10–48.
39. Sefton, A.J., Dreher, B., Harvey, A., and Paxinos, G. (2004). Visual system. In *The Rat Nervous System*, 3rd Edition, G. Paxinos, ed. (Burlington: Academic Press), pp. 1083–1165.
40. Sterratt, D.C., Lyngholm, D., Willshaw, D.J., and Thompson, I.D. (2013). Standard anatomical and visual space for the mouse retina: computational reconstruction and transformation of flattened retinæ with the Retistruct package. *PLoS Comput. Biol.* 9, e1002921.
41. Dräger, U.C., and Olsen, J.F. (1981). Ganglion cell distribution in the retina of the mouse. *Invest. Ophthalmol. Vis. Sci.* 20, 285–293.
42. Jeon, C.J., Strettoi, E., and Masland, R.H. (1998). The major cell populations of the mouse retina. *J. Neurosci.* 18, 8936–8946.
43. Salinas-Navarro, M., Jiménez-López, M., Valiente-Soriano, F.J., Alarcón-Martínez, L., Avilés-Trigueros, M., Mayor, S., Holmes, T., Lund, R.D., Villegas-Pérez, M.P., and Vidal-Sanz, M. (2009). Retinal ganglion cell population in adult albino and pigmented mice: a computerized analysis of the entire population and its spatial distribution. *Vision Res.* 49, 637–647.
44. Wässle, H., Peichl, L., and Boycott, B.B. (1981). Morphology and topography of on- and off-alpha cells in the cat retina. *Proc. R. Soc. Lond. B Biol. Sci.* 212, 157–175.
45. Chang, L., Breuninger, T., and Euler, T. (2013). Chromatic coding from cone-type unselective circuits in the mouse retina. *Neuron* 77, 559–571.
46. Ecker, J.L., Dumitrescu, O.N., Wong, K.Y., Alam, N.M., Chen, S.K., LeGates, T., Renna, J.M., Prusky, G.T., Berson, D.M., and Hattar, S. (2010). Melanopsin-expressing retinal ganglion-cell photoreceptors: cellular diversity and role in pattern vision. *Neuron* 67, 49–60.
47. Estevez, M.E., Fogerson, P.M., Ilardi, M.C., Borghuis, B.G., Chan, E., Weng, S., Auferkorte, O.N., Demb, J.B., and Berson, D.M. (2012). Form and function of the M4 cell, an intrinsically photosensitive retinal ganglion cell type contributing to geniculocortical vision. *J. Neurosci.* 32, 13608–13620.
48. Peichl, L. (1989). Alpha and delta ganglion cells in the rat retina. *J. Comp. Neurol.* 286, 120–139.
49. Farrow, K., Teixeira, M., Szikra, T., Viney, T.J., Balint, K., Yonehara, K., and Roska, B. (2013). Ambient illumination toggles a neuronal circuit switch in the retina and visual perception at cone threshold. *Neuron* 78, 325–338.
50. Huberman, A.D., Wei, W., Elstrott, J., Stafford, B.K., Feller, M.B., and Barres, B.A. (2009). Genetic identification of an On-Off direction-selective retinal ganglion cell subtype reveals a layer-specific subcortical map of posterior motion. *Neuron* 62, 327–334.
51. Münch, T.A., da Silveira, R.A., Siegert, S., Viney, T.J., Awatramani, G.B., and Roska, B. (2009). Approach sensitivity in the retina processed by a multifunctional neural circuit. *Nat. Neurosci.* 12, 1308–1316.